Aureolegraph internal scattering correction

John DeVore,[1,*] Dennis Villanucci,[2] and Andrew LePage[2]

[1]Applied Physics Group, Visidyne, Inc., 429 Stanley Drive, Santa Barbara, California 93105, USA

[2]Applied Physics Group, Visidyne, Inc., 99 South Bedford St., Suite #107, Burlington, Massachusetts 01803, USA

*Corresponding author: devore@visidyne.com

Received 21 August 2012; accepted 4 October 2012;
posted 18 October 2012 (Doc. ID 174697); published 13 November 2012

Two methods of determining instrumental scattering for correcting aureolegraph measurements of particulate solar scattering are presented. One involves subtracting measurements made with and without an external occluding ball and the other is a modification of the Langley Plot method and involves extrapolating aureolegraph measurements collected through a large range of solar zenith angles. Examples of internal scattering correction determinations using the latter method show similar power-law dependencies on scattering, but vary by roughly a factor of 8 and suggest that changing aerosol conditions during the determinations render this method problematic. Examples of corrections of scattering profiles using the former method are presented for a range of atmospheric particulate layers from aerosols to cumulus and cirrus clouds.

OCIS codes: 010.0280, 280.1310, 290.1310, 290.2558, 290.5820.

1. Introduction

Solar coronagraphs [1] and our Sun and Aureole Measurement (SAM) cloud aureolegraph [2] face the same problem of imaging relatively dim objects, coronas or aureoles, respectively, in the presence of the Sun, which is 5 to 6 orders of magnitude brighter. Coronagraphs accomplish this using a sophisticated optical system involving a Lyot stop [3] while our SAM aureolegraph employs a simpler optical system that focuses the solar disk and aureole onto an imaging surface with a hole though which the solar disk radiance passes into a beam dump. The SAM design requires less accurate pointing since active feedback from its companion solar disk imager, which achieves better than 1 pixel (0.015°) pointing accuracy under clear skies, becomes ineffective as increasing cloud optical depth obscures the edge of the solar disk. A penalty for SAM's simple optical design is some residual instrumental scattering in its aureolegraph that must be characterized and modeled in order to correct aureole profile measurements.

1559-128X/12/337891-09$15.00/0

O'Neill and Miller [4] characterized the instrumental scattering of their narrow field-of-view scanning radiometer, which was designed to measure solar beam extinction and aureole-scattered radiance, by mimicking the appearance of the Sun in the absence of atmospheric scattering in their laboratory. However, their calibration system requires a large distance between the radiometer and a collimated laboratory source, which must be very bright. The AERONET network [5] uses the Langley Plot technique [6] to calibrate reference Sun photometers at the Mauna Loa Observatory above the atmospheric boundary layer (where most areosols reside). The reference instruments are then used as secondary standards to calibrate instruments used at AERONET sites around the world. AERONET uses a 2 m integrating sphere to calibrate the sky photometers of both reference and field instruments. We use an integrating sphere to calibrate both the solar disk imager and aureolegraph of SAM instruments and then fine tune the calibration of the solar disk imagers through cross comparison with a nearby AERONET instrument.

We have developed two methods to determine the internal scattering profiles of SAM aureolegraphs.

Section 2 discusses internal scattering and the correction we apply to SAM aureole profiles. Section 3 describes a method for measuring the internal scattering profile using an external occulter and Section 4 a method that uses a modification of the Langley Plot technique. Section 5 shows some examples of correcting SAM aureole profiles, and Section 6 concludes with a summary.

2. Internal Scattering Correction

The radiance measured by a SAM aureolegraph, $L_{\text{sam}}(\theta,\mu_s)$, is composed of sunlight scattered by atmospheric particles and to a much lesser extent molecules, $L_{\text{sca}}(\theta,\mu_s)$, and sunlight scattered internally within the instrument itself, $L_{\text{int}}(\theta,\mu_s)$:

$$L_{\text{sam}}(\theta,\mu_s) = L_{\text{sca}}(\theta,\mu_s) + L_{\text{int}}(\theta,\mu_s), \tag{1}$$

where θ is the scattering angle and μ_s the cosine of the solar zenith angle. The equation for the radiance $L_{\text{single-scatter}}(\theta,\mu_s)$ single-scattered by atmospheric particles and molecules in a uniform, plane-parallel layer is given by Liou [7]:

$$L_{\text{single-scatter}}(\theta,\mu_s) = I_{\text{sun}}(\lambda)\exp(-\tau_{\text{tot}}/\mu_s) \times \left[\frac{\tau_{\text{par}}}{\mu_s}\frac{\varpi P_{\text{par}}(\theta)}{4\pi} + \frac{\tau_{\text{ray}}}{\mu_s}\frac{P_{\text{ray}}(\theta)}{4\pi}\right], \tag{2}$$

where $I_{\text{sun}}(\lambda)$ is the exoatmospheric solar irradiance at the time of the measurement and in a 0.010 μm band centered at wavelength λ. For most SAM instruments, particularly those used for cloud research, $\lambda = 0.67$ μm. This value of λ is assumed in the remainder of the paper. τ_{tot} is the total extinction optical depth. The major contributor to τ_{tot} is the particulate scattering optical depth τ_{par}, followed by the optical depth for Rayleigh scattering from molecules τ_{ray}. For completeness, we include the optical depth for absorption by molecules, τ_{abs}, so that $\tau_{\text{tot}} = \tau_{\text{par}} + \tau_{\text{ray}} + \tau_{\text{abs}}$. Using Nicolet's [8] empirical formula for the Rayleigh scattering cross section and a surface pressure of 1000 hPa, $\tau_{\text{ray}} = 0.043$. For $\lambda = 0.67$ μm the optical depth for absorption by water vapor is negligible and by ozone is slightly larger than 0.01, which is comparable to the accuracy of SAM optical depth measurements, and therefore we take $\tau_{\text{abs}} \approx 0$ in this analysis. ϖ is the single scatter albedo (the ratio of the scattering to the extinction cross section). ϖ is 1 for Rayleigh scattering [which is why this factor is omitted from the term in Eq. (2)], typically close to 1 for clouds in the visible, but can be significantly less than 1 for aerosols. $P_{\text{par}}(\theta)$ is the particulate scattering phase function and $P_{\text{ray}}(\theta)$ is the molecular scattering phase function, which is given by Rayleigh's formula [7], $P_{\text{ray}}(\theta) = (3/4)[1+\cos^2(\theta)]$. Figure 1 shows a plot of $P_{\text{ray}}(\theta)$ and an example of $\varpi P_{\text{par}}(\theta)$ for aerosols. Over the range of scattering angles of interest, $0.6° \le \theta \le 8°$, $P_{\text{ray}}(\theta)$, and $\varpi P_{\text{par}}(\theta)$ are within a factor of 10 of each other.

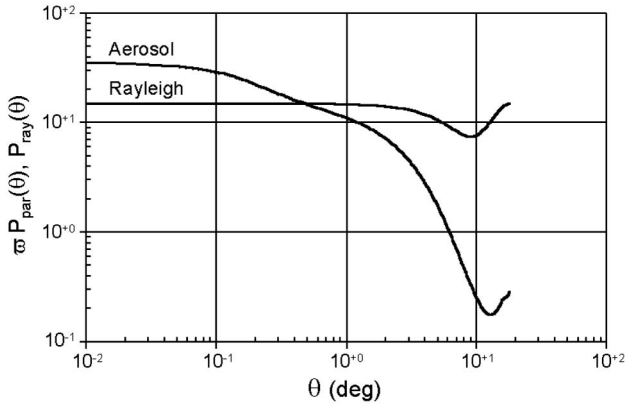

Fig. 1. Plot comparing $P_{\text{ray}}(\theta)$ and an example of $\varpi P_{\text{par}}(\theta)$ from the AERONET inversion at the ARM SGP site at 18.636 UT on 10 January 2008, for $\lambda = 0.67$ μm.

Since, as Dave has shown [9], two orders of scattering are required even for $\tau_{\text{ray}} \approx 0.05$ and more orders for larger τ_{ray}, we developed a correction for single scattering based on numerical calculations for the scattering of sunlight incident normally on a uniform, plane-parallel molecular atmosphere for scattering angles (relative to normal) from 0° to 8°. We used the successive orders of scattering method [10] using the Monte Carlo method [11] to calculate the integrals involved. Since the scattering angles of interest are close to the Sun, we also included the angular spread of the emitted sunlight using the solar limb model of Hestroffer and Magnan [12]. The albedo of the ground was taken as 0.2. Figure 2 shows the ratio of computed multiple-scattering to single-scattering radiance $\rho(\theta) = L_{\text{ms}}(\theta)/L_{\text{ss}}(\theta)$ for Rayleigh scattering in the absence of particulates. It also shows the results for an atmosphere with only aerosols using $\varpi P_{\text{par}}(\theta)$ from the AERONET inversion of data for $\lambda = 0.67$ μm from the Atmospheric Radiation Measurement (ARM) Southern Great Plains (SGP) site at 18.636 UT on 10 January 2008. $L_{\text{ms}}(\theta)$ includes 30 orders of scattering, since examination of calculations with fewer orders of scattering included

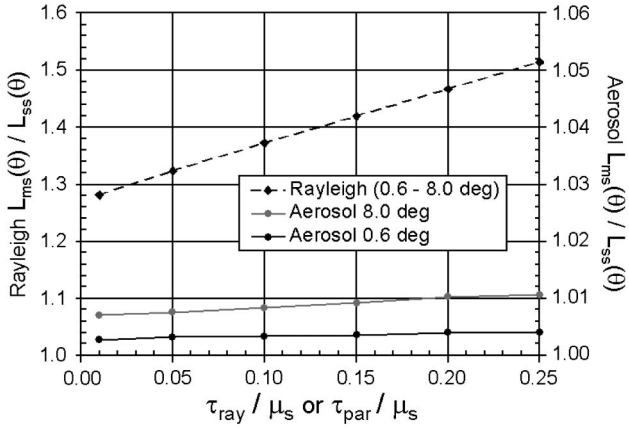

Fig. 2. Multiplicative factor to correct single-scattering radiance to multiple-scattering for Rayleigh scattering for $0.6° \le \theta \le 8.0°$ and aerosol scattering for $\theta = 0.6°$, 8.0°.

shows that 30 orders of scattering is more than sufficient to achieve convergence of the results for the range of optical depths of interest in this work. For $0° \le \theta \le 8°$ the standard deviation of the computed multiple scattering correction for Rayleigh scattering $\rho_{\text{ray}}(\theta)$ is less than 0.2% for $0 \le \tau_{\text{ray}}/\mu_s \le 0.2$, indicating that the correction is not a function of θ in the forward direction. By way of contrast, the multiple scattering correction for the aerosol case for $\tau_{\text{par}}/\mu_s = 0.25$ increases with θ but is significantly smaller than for the Rayleigh case—less than 0.5% for $\theta = 0.6°$ and roughly 1% for $\theta = 8.0°$. Therefore, for the purposes of this work we ignore the error caused by particulate multiple scattering and take Rayleigh multiple scattering into account using a least-squares fit to numerical calculations (not shown) over the range from $\tau_{\text{ray}}/\mu_s = 0.01$ to $\tau_{\text{ray}}/\mu_s = 1.00$:

$$\rho_{\text{ray}}\left(\frac{\tau_{\text{ray}}}{\mu_s}\right) \approx 1.281 + 0.8641\left(\frac{\tau_{\text{ray}}}{\mu_s}\right) + 0.2264\left(\frac{\tau_{\text{ray}}}{\mu_s}\right)^2. \tag{3}$$

The Pearson product moment coefficient for this fit is $r = 0.9993$. Using $\rho_{\text{ray}}(\tau/\mu_s)$ to correct the Rayleigh scattering term and ignoring the small particulate multiple scattering correction in Eq. (2) we approximate the scattered radiance $L_{\text{sca}}(\theta, \mu_s)$ as follows:

$$L_{\text{sca}}(\theta, \mu_s) \approx I_{\text{sun}}(\lambda)\exp(-\tau_{\text{tot}}/\mu_s) \times \left[\frac{\tau_{\text{par}}}{\mu_s}\frac{\varpi P_{\text{par}}(\theta)}{4\pi} + \rho_{\text{ray}}(\tau_{\text{ray}}/\mu_s)\frac{\tau_{\text{ray}}}{\mu_s}\frac{P_{\text{ray}}(\theta)}{4\pi}\right]. \tag{4}$$

The radiance reaching the SAM aureolegraph aperture that can give rise to $L_{\text{int}}(\theta)$ is the combination of $L_{\text{sca}}(\theta)$ and the direct solar beam attenuated by the total atmospheric extinction, $L_{\text{dir}}(\theta, \mu_s)$, which can be approximated as

$$L_{\text{dir}}(\theta, \mu_s) = I_{\text{sun}}(\lambda)\exp(-\tau_{\text{tot}}/\mu_s)\frac{\delta(\theta)}{4\pi}, \tag{5}$$

where δ is the Dirac delta function.

From Eq. (4) note that $L_{\text{sca}}(\theta, \mu_s)$ peaks for $\tau_{\text{tot}}/\mu_s \approx \tau_{\text{par}}/\mu_s \gtrsim 1$, while from Eq. (5) $L_{\text{dir}}(\theta, \mu_s)$ monotonically decreases with τ_{tot}/μ_s. As a consequence it should not be surprising that $L_{\text{int}}(\theta, \mu_s)$ is most important when τ_{tot}/μ_s is small. Also, since $L_{\text{sca}}(\theta, \mu_s)$ is diffuse while $L_{\text{dir}}(\theta, \mu_s)$ is concentrated, it is the latter component that gives rise to internal scattering. Therefore we are led to approximate $L_{\text{int}}(\theta, \mu_s)$ as

$$L_{\text{int}}(\theta, \mu_s) \approx I_{\text{sun}}(\lambda)\exp(-\tau_{\text{tot}}/\mu_s)S_{\text{int}}(\theta), \tag{6}$$

where $S_{\text{int}}(\theta)$ is a normalized, internal scattering function, which can be applied to correct $L_{\text{sam}}(\theta, \mu_s)$ to give $L_{\text{sca}}(\theta, \mu_s)$ by simply inverting Eq. (1) and using Eq. (6):

$$L_{\text{sca}}(\theta, \mu_s) = L_{\text{sam}}(\theta, \mu_s) - I_{\text{sun}}(\lambda)\exp(-\tau_{\text{tot}}/\mu_s)S_{\text{int}}(\theta), \tag{7}$$

where $I_{\text{sun}}(\lambda)\exp(-\tau_{\text{tot}}/\mu_s)$ is measured by SAM's solar disk imager. Or, if we want to find the particulate scattered radiance $L_{\text{par}}(\theta, \mu_s)$, then we need to correct $L_{\text{sca}}(\theta, \mu_s)$ by subtracting the Rayleigh scattered radiance:

$$L_{\text{par}}(\theta, \mu_s) = L_{\text{sam}}(\theta, \mu_s) - I_{\text{sun}}(\lambda)\exp(-\tau_{\text{tot}}/\mu_s) \times \left[S_{\text{int}}(\theta) + \rho_{\text{ray}}(\tau_{\text{ray}}/\mu_s)\frac{\tau_{\text{ray}}}{\mu_s}\frac{P_{\text{ray}}(\theta)}{4\pi}\right]. \tag{8}$$

The next two sections describe two different ways of determining $S_{\text{int}}(\theta)$ for SAM.

3. Ball-and-Stick Method

Consider Eqs. (1) and (7) further. If the direct solar beam is blocked from illuminating the aureolegraph by placing an object, for example a ball on the end of a long stick, so as to shade the aperture, then $I_{\text{sun}} = 0$ and the occluded radiance measurement $L_{\text{occ}}(\theta)$ includes only the contribution from atmospheric scattering $L_{\text{sca}}(\theta)$. On a clear day when atmospheric conditions are stable, we subtract measurements without $[L_{\text{sam}}(\theta)]$ and with $[L_{\text{occ}}(\lambda)]$ the occluding ball and calculate $S_{\text{int}}(\theta)$ by solving Eq. (7) for the latter quantity:

$$S_{\text{int}}(\theta) = \frac{L_{\text{sam}}(\theta, \mu_s) - L_{\text{occ}}(\theta, \mu_s)}{I_{\text{sun}}(\lambda)\exp(-\tau_{\text{tot}}/\mu_s)}, \tag{9}$$

where again, $I_{\text{sun}}(\lambda)\exp(-\tau_{\text{tot}}/\mu_s)$ is provided by the (unobscured) SAM solar disk imager. Figure 3 illustrates the ball-and-stick, hereafter BAS, measurement setup. A black styrofoam ball, approximately 8 cm in diameter, is attached to a long pole and located ~5 m from the SAM aureolegraph so that it casts a shadow slightly larger than the aureolegraph entrance aperture. The ~5 m range is required so

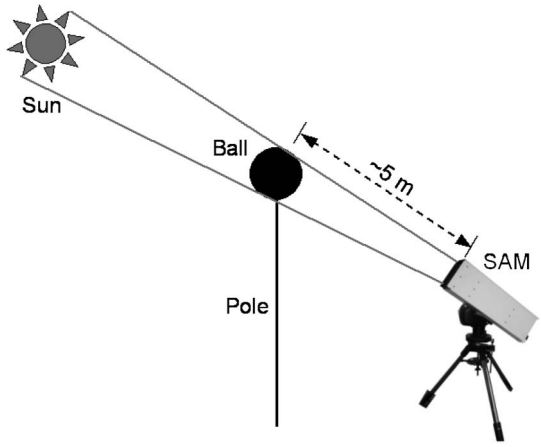

Fig. 3. Illustration of instrument setup for ball-and-stick measurements.

that the ball is nearly in focus on the aureolegraph imaging screen. Data are then taken for approximately 2–3 min while the ball completely shades the aperture. Immediately afterward the ball is removed and an additional 2–3 min of data are acquired without the obscuration. Data from the solar disk imager, which remains unobscured, are acquired during both operations. Typically BAS measurements are taken on a still (no blowing dust or debris), clear day. Nevertheless, because it is somewhat difficult to keep the ball positioned correctly shading the aureolegraph aperture, it is necessary to review the occluded images to check the alignment. This process involves reviewing either the images or the horizontal and vertical traces in the level 1.0 processed data. Data exhibiting profiles significantly different, e.g., higher or lopsided, are excluded.

As an example, consider the BAS data collected on 8 January 2010, at the Department of Energy's ARM SGP facility by SAM #300. This day was very clear with $\tau_{\mathrm{par}} \approx 0.046 \pm 0.003$. Figure 4 shows that after the first couple of measurements there was a very slight downward trend in τ_{par} of ~0.001 hr^{-1}. Figure 5 shows two examples of solar disk and aureole radiance profiles. The occluded profile represents the average of seven measurements between 16.89 and 16.96 UT. Three profiles were excluded from the average because they showed indications that the ball was not properly centered in line with the aureolegraph aperture. The nonoccluded profile represents the average of 16 measurements between 16.81 and 17.02 UT. The error bars in the plot represent the standard deviations of the measurements at the same angle, but are too small (~0.004 and ~0.003, respectively) to show up in the plot. The nonoccluded radiance ranges from a factor of six brighter near 0.6° to only 6% at 7.8°. Although the magnitude of $L_{\mathrm{int}} = L_{\mathrm{sam}} - L_{\mathrm{occ}}$ decreases as $\tau_{\mathrm{par}}/\mu_s$ increases, it can remain noticeable for $\tau_{\mathrm{par}}/\mu_s \lesssim 1$ depending upon the size distribution of the particulates forming the aureole. Figure 5 also shows the averaged solar disk radiance profile. These data were used to calculate

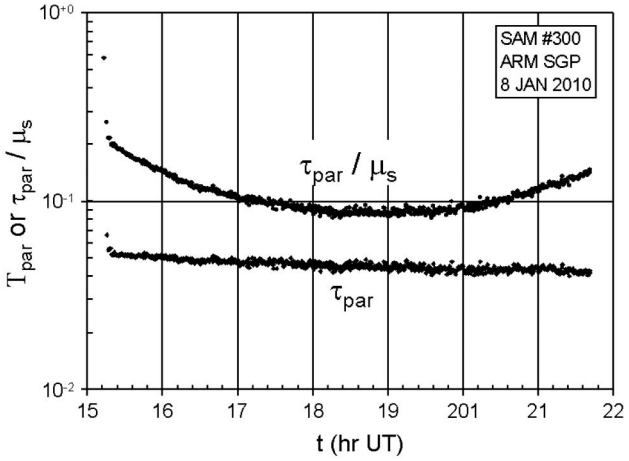

Fig. 4. Particulate optical depth measured by SAM #300 at the ARM SGP site on 8 January 2010.

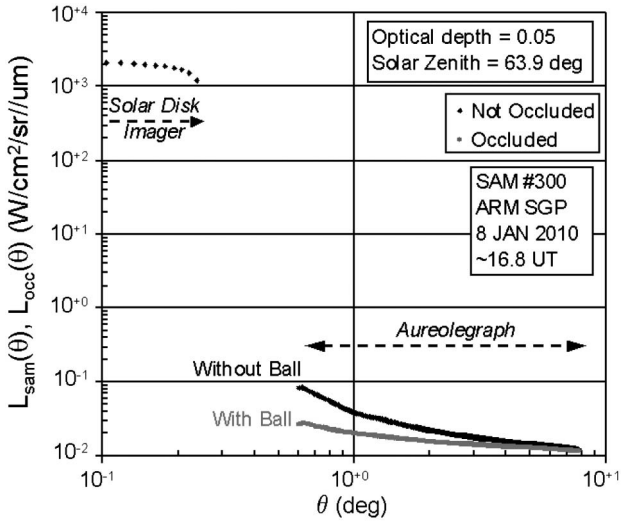

Fig. 5. Solar disk and aureole radiance profiles collected around 16.8 UT on 8 January 2010 at the ARM SGP site by SAM #300 with and without an occluding ball.

τ_{tot} and τ_{par}. Figure 6 shows the values of $S_{\mathrm{int}}(\theta)$ calculated using Eq. (9). With the ordinate scale expanded and taking into consideration the subtraction of two measurements in Eq. (9), the error bars on $S_{\mathrm{int}}(\theta)$ (~0.004) are apparent in the plot for $\theta \gtrsim 1°$. $S_{\mathrm{int}}(\theta)$ has the form of a power-law function of θ with slope of approximately −2. This slope is shallower than that of diffraction from a circular aperture as represented by an Airy function [13], which has an asymptotic power-law slope of −3.

As a consistency check we use $S_{\mathrm{int}}(\theta)$ calculated using the BAS method (Fig. 6) to correct SAM aureole profiles [using Eq. (8)] at two times, $t = 15.881$ and $t = 21.776$ hr UT, that have the same particulate optical thickness, $\tau_{\mathrm{par}}/\mu_s = 0.15$, but are earlier and later than the data used to determine the correction. The plot in Fig. 7 shows that the earlier scattering profile has less forward scattering and less scattering

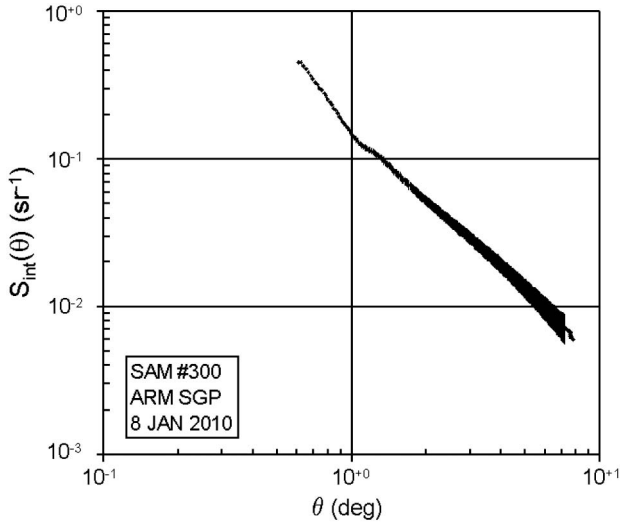

Fig. 6. Internal scattering function calculated using Eq. (9) and the data shown in Fig. 5.

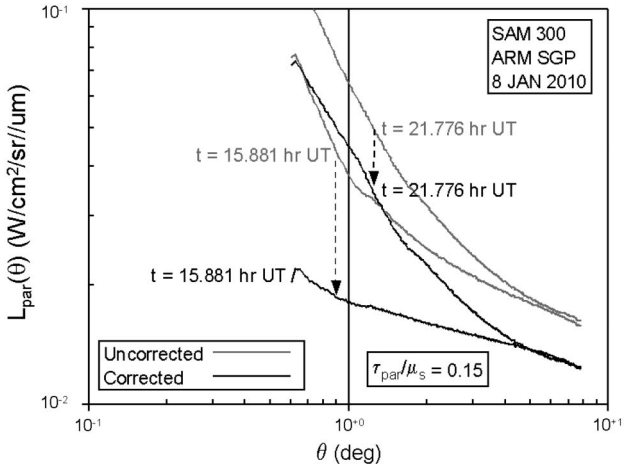

Fig. 7. Examples of uncorrected (gray) and corrected (black) particulate scattering profiles $L_{\mathrm{par}}(\theta)$ for 8 January 2009 at 15.881 and 21.776 UT, both for $\tau_{\mathrm{par}}/\mu_s \approx 0.15$.

overall than the later one. This finding is consistent with the AERONET phase function retrievals shown in Fig. 8. Noisy measurements near the edge of the aureolegraph beam dump, i.e., for $\theta \lesssim 0.64°$, give rise to the slight region with positive slope and should be discounted.

4. Modified Langley Plot Method

Motivated by the success and elegance of the Langley Plot technique [6] for calibrating sun photometers we looked for a similar approach for determining $S_{\mathrm{int}}(\theta)$. Substituting $L_{\mathrm{sca}}(\theta,\mu_s)$ from Eq. (4) for $L_{\mathrm{sam}}(\theta,\mu_s)$ and $L_{\mathrm{int}}(\theta,\mu_s)$ from Eq. (6) into Eq. (1) and dividing by $I_{\mathrm{sun}}(\lambda)\exp(-\tau_{\mathrm{tot}}/\mu_s)$ gives

$$\frac{L_{\mathrm{sam}}(\theta,\mu_s)}{I_{\mathrm{sun}}(\lambda)\exp(-\tau_{\mathrm{tot}}/\mu_s)} = \left[\frac{\tau_{\mathrm{par}}}{\mu_s}\frac{\varpi P_{\mathrm{par}}(\theta)}{4\pi} + \rho(\tau_{\mathrm{ray}}/\mu_s) \times \frac{\tau_{\mathrm{ray}}}{\mu_s}\frac{P_{\mathrm{ray}}(\theta)}{4\pi}\right] + S_{\mathrm{int}}(\theta). \quad (10)$$

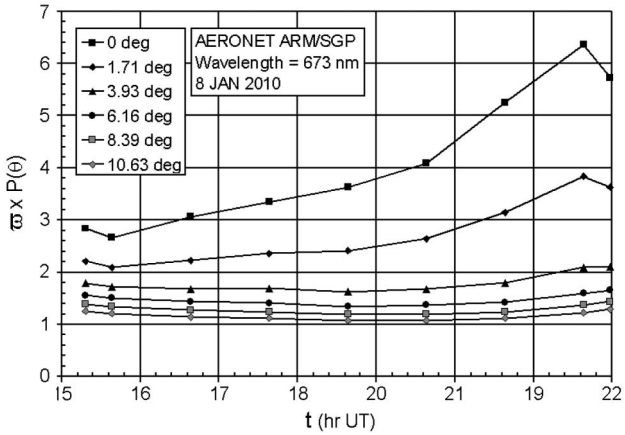

Fig. 8. Plot of $\varpi P_{\mathrm{par}}(\theta)$ versus time for $0° \le \theta \le 10.63°$ based on the AERONET retrievals of ϖ and $P_{\mathrm{par}}(\theta)$ at the ARM SGP site on 8 January 2010 for $\lambda = 0.67$ μm.

Define the SAM measurement profile, $S_{\mathrm{sam}}(\theta,\mu_s)$, as the ratio of a SAM aureolegraph measurement to a SAM solar disk imager measurement less a correction for Rayleigh scattering:

$$S_{\mathrm{sam}}(\theta,\mu_s) \equiv \frac{L_{\mathrm{sam}}(\theta,\mu_s)}{I_{\mathrm{sun}}(\lambda)\exp(-\tau_{\mathrm{tot}}/\mu_s)} - \rho(\tau_{\mathrm{ray}}/\mu_s)\frac{\tau_{\mathrm{ray}}}{\mu_s}\frac{P_{\mathrm{ray}}(\theta)}{4\pi}. \quad (11)$$

Substitute Eq. (11) into Eq. (10) to find

$$S_{\mathrm{sam}}(\theta,\mu_s) = \frac{\tau_{\mathrm{par}}}{\mu_s}\frac{\varpi P_{\mathrm{par}}(\theta)}{4\pi} + S_{\mathrm{int}}(\theta), \quad (12)$$

where for each value of θ, the left-hand side represents a SAM measurement and the right-hand side is a linear function of $\tau_{\mathrm{par}}\varpi P_{\mathrm{par}}(\theta)/\mu_s$. τ_{par} and μ_s are known from SAM solar disk imager measurements. If $\varpi P_{\mathrm{par}}(\theta)$ turns out to be independent of time during the SAM measurements, then for each θ we could perform a linear least squares fit of $S_{\mathrm{sam}}(\theta,\mu_s)$ as a function of $\tau_{\mathrm{par}}/\mu_s$. The y axis intercept thus found would be $S_{\mathrm{int}}(\theta)$.

Figure 8 shows a plot of $\varpi P_{\mathrm{par}}(\theta)$ as a function of time from the inversion [14,15] of the AERONET aerosol data at the ARM SGP site on 8 January 2010. Although the temporal variation of $\varpi P_{\mathrm{par}}(\theta)$ decreases as θ decreases, it is appreciable over the angular range of SAM aureole measurements. We have allowed for temporal variation in our analysis by assuming that $\varpi P_{\mathrm{par}}(\theta)$ varies linearly with time:

$$\varpi P_{\mathrm{par}}(\theta) \approx \varpi_0 P_0(\theta)[1 + \beta(\theta)(t - t_0)], \quad (13)$$

where $\beta(\theta)$ is the average, fractional rate of change of $\varpi_0 P_0(\theta)$ with time. We substitute Eq. (13) into Eq. (12) to find

$$S_{\mathrm{sam}}(\theta,\mu_s) = \frac{\varpi_0 P_0(\theta)}{4\pi}[1 + \beta(\theta)(t - t_0)]\left(\frac{\tau_{\mathrm{par}}(t)}{\mu_s(t)}\right) + S_{\mathrm{int}}(\theta). \quad (14)$$

In order to determine the value of $\beta(\theta)$ for each θ that best fits the SAM measurements in a least squares sense, we define a column optical depth corrected for the time dependence of $\varpi P_{\mathrm{par}}(\theta)$ as

$$\tau_{\mathrm{cor}}(t) \equiv \frac{\tau_{\mathrm{par}}(t)[1 + \beta(\theta)(t - t_0)]}{\mu_s(t)}. \quad (15)$$

Using Eq. (15), Eq. (14) becomes

$$S_{\mathrm{sam}}(\theta,\mu_s) = \frac{\varpi_0 P_0(\theta)}{4\pi}\tau_{\mathrm{cor}}(t) + S_{\mathrm{int}}(\theta). \quad (16)$$

Equation (16) is a linear function of $\tau_{\mathrm{cor}}(t)$. Given a value of $\beta(\theta)$, which determines $\tau_{\mathrm{cor}}(t)$, we solve

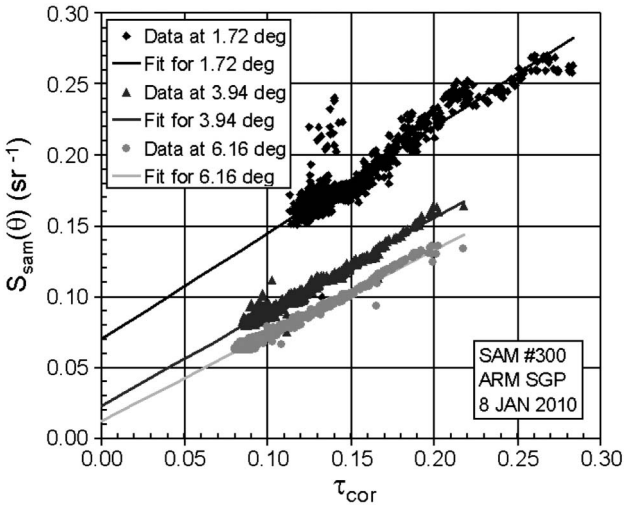

Fig. 9. Plots of SAM radiance L_{sam} normalized by the solar irradiance at the aureolegraph aperture $I_{sun}\exp(-\tau_{tot}/\mu_s)$ as a function of corrected column optical depth τ_{cor} for $\theta = 1.72°$, 3.94°, and 6.16° and corresponding best fits.

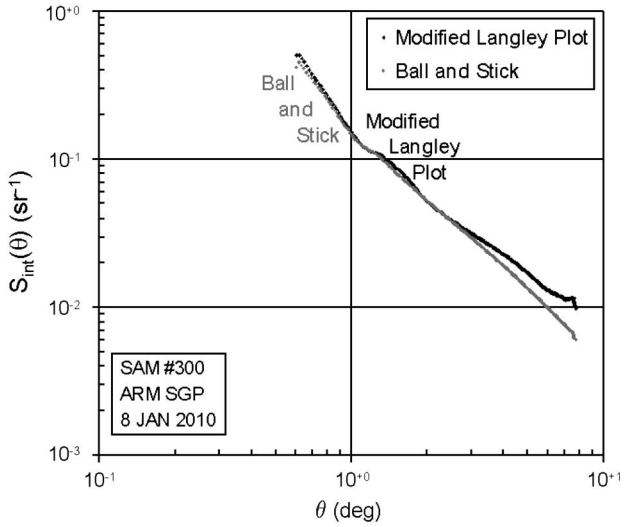

Fig. 11. Internal scattering functions calculated using Eq. (14) (black diamonds, MLP method) and Eq. (9) (gray dots, BAS Method) for the 8 June 2010 ARM SGP SAM dataset.

Eq. (16) using the method of least squares [16] weighting all of the $S_{sam}(\theta,\mu_s)$ measurements equally. We perform a simple, brute-force search for the value of $\beta(\theta)$ between −2 and 2 hr^{-1} that provides the best fit to the SAM data for each θ. The symbols in Fig. 9 show the $S_{sam}(\theta)$ data for ARM/SGP on 8 January 2010, plotted as a function of τ_{cor} for $\theta = 1.72°$, 3.94°, and 6.16°. The lines in the figure are the best fits. The Pearson r statistics [16] for the $\beta(\theta)$ fits are 0.942, 0.986, and 0.993 for $\theta = 1.72°$, 3.94°, and 6.16°, respectively. The intersections of the lines with the y axis give the internal scattering function $S_{int}(\theta)$ at each θ. As expected, $\varpi P_{par}(\theta)$ changes most rapidly for small θ and tends to 0 for $\theta \gtrsim 4°$. Figure 10 shows the values we found for $\beta(\theta)$ from the search. The small black diamonds in Fig. 11 show the values of $S_{int}(\theta)$ found from applying the modified Langley Plot (MLP) method to the 8 January 2010 ARM SGP SAM dataset. For comparison, the small gray dots in the figure repeat the values of $S_{int}(\theta)$ from Fig. 6 found using the BAS method. The results of the two methods agree to 20% or better for $\theta \lesssim 4°$. However, at low optical thicknesses such errors can be significant.

Errors in the forward scattering correction raise questions as to how precisely $S_{int}(\theta)$ can be determined and how rapidly it may change with time. To begin to address these issues we calculated $S_{int}(\theta)$ for SAM #300 at the ARM SGP site using the MLP method for 9 days between 3 November 2009, and 25 March, 2010, that appeared sufficiently clear and stable to permit the MLP method to work. Figure 12 shows the results for these days. The calculations show similar, roughly power-law behaviors with slopes slightly less negative than −2 but with a spread in amplitude of about a factor of 8. $S_{int}(\theta)$ for 8 January 2010, the day selected for the BAS measurements, is one of the lowest curves. SAM maintenance instructions recommend minimizing the effects of sunlight scattering from the sensor window (1) by

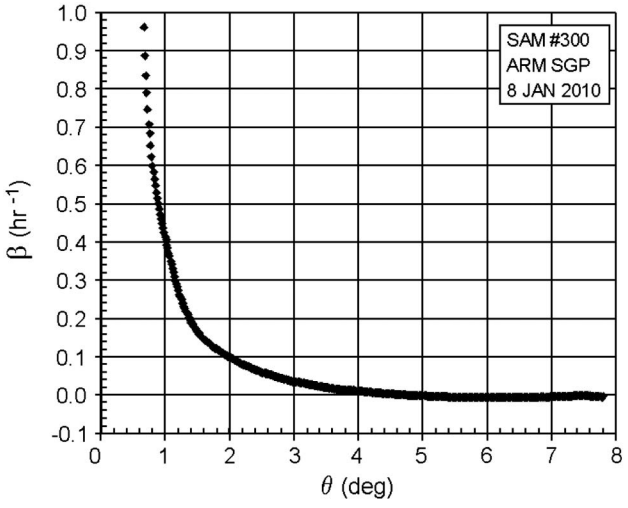

Fig. 10. Plot of $\beta(\theta)$ as a function of θ found using the MLP method.

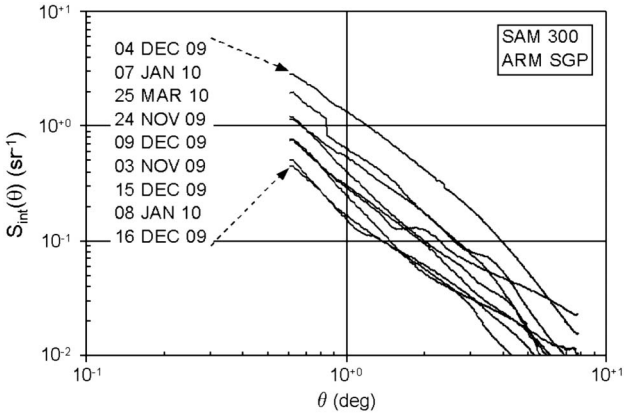

Fig. 12. Examples of $S_{int}(\theta)$ calculated using the MLP method over a period of nearly half a year at the ARM SGP site.

preventing dust or dirt from collecting on the window and (2) by gently cleaning the window with a soft (camel hair) brush or air duster, or using an optical cleaning solution (nonresidue forming) with a clean, lint-free cloth. The instructions also recommend replacing the window with a new one once a month. If more BAS measurements had been made during this period, then a comparison of the results of the two methods could provide clues as to the source of the variability in $S_{\text{int}}(\theta)$, e.g., whether from inadequate cleaning or other problems. That the plot does not show an obvious trend with time suggests that the problem may lie in the assumed stability or regularity of $\varpi P_{\text{par}}(\theta)$ that is not well modeled with a simple linear dependence on time during the measurements used to determine $S_{\text{int}}(\theta)$. A cursory visual examination of plots similar to Fig. 8 for the days involved is consistent with this hypothesis.

5. Examples

In this section we look at a number of examples of correcting SAM profiles for internal scattering to see when it is important. We use $S_{\text{int}}(\theta)$ calculated using the BAS method (Fig. 6) and start with a difficult case, the correction of aerosol scattering profiles. These are difficult both because aerosol optical depths can be quite low and because aerosol phase functions can have broad, shallow forward peaks. We consider aerosol scattering on 12 February 2010, at the ARM SGP site. The particulate optical depth varied from 0.05 to 0.22 over the course of the day, peaking in the afternoon around 21:15 UT. Figure 13 shows three examples, illustrating the range of τ_{par}/μ_s from 0.10 to 0.35. In all three cases the forward peaks of the profiles are significantly diminished, by up to a factor of 2.2 for $\tau_{\text{par}} = 0.10$ to 1.7 for $\tau_{\text{par}} = 0.35$. The corrections are largest for the smallest scattering angles.

Moving up in particle size, we next consider examples of the correction of particle scattering profiles on 26 May 2010, a day with a variety of clouds ranging from fair weather cumulus to cirrus. Figure 14 compares three examples of uncorrected and corrected thin cumulus scattering profiles with an aerosol example. While the maximum correction in the aerosol case ($\tau_{\text{par}}/\mu_s = 0.19$) is 20%, it drops from 6% for the thinner cumulus cases ($\tau_{\text{par}}/\mu_s = 0.40, 0.80$) to 2% for the thickest ($\tau_{\text{par}}/\mu_s = 1.20$). As with the aerosols, the corrections are largest for the smallest angles.

For situations in which particulate scatterers are large compared with λ, i.e., for clouds, the diffraction approximation [17] relates the differential column density of scatterers $n(a)$ cm^{-2} μm^{-1} as a function of radius a μm to the negative gradient of the scattered radiance profile $L_{\text{par}}(\theta, \mu_s)$:

$$n(a) = -\frac{4\theta^6 \mu_s}{e^{-\tau_{\text{los}}} I_{\text{sun}} \lambda^3} \frac{dL_{\text{par}}(\theta)}{d\theta}, \tag{17}$$

where $a = \lambda/2\theta$, the single scattering approximation is assumed to apply, and the factor of μ_s in the numerator adjusts $n(a)$ to apply to the vertical. The particulates are also assumed to be spherical or quasi-spherical, which is reasonable even for small ice crystals in cirrus [18]. We compared calculations of the particulate size distributions using the diffraction approximation to the three cumulus cases shown in Fig. 14. The calculations using the profiles not corrected for internal scattering averaged from 3.2% larger for $\tau_{\text{los}} = 0.40$ to 0.8% larger for $\tau_{\text{los}} = 1.2$, with standard deviations of 9.1% and 1.3%, respectively.

Finally we consider a cirrus case. Figure 15 compares four examples of uncorrected and corrected scattering profiles for thin cirrus clouds. The corrections range from a maximum of about 13% for the thinnest case ($\tau_{\text{par}}/\mu_s = 0.16$) to 4% for the thickest case ($\tau_{\text{par}}/\mu_s = 0.49$). However, unlike the previous examples, the correction is largest for the larger scattering angles rather than the smaller ones. The errors in diffraction approximation calculations

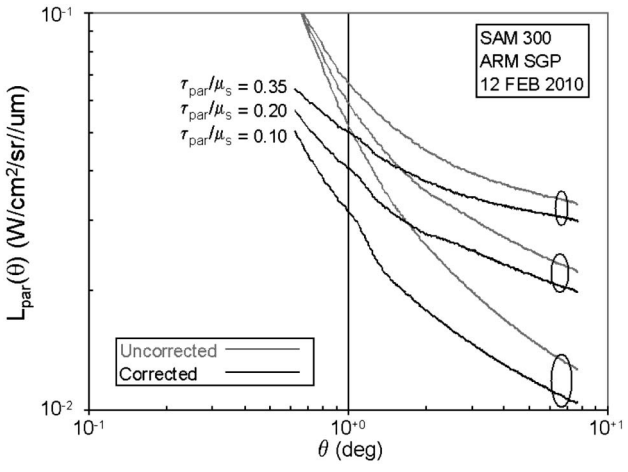

Fig. 13. Examples of uncorrected (gray) and corrected (black) particulate scattering profiles $L_{\text{par}}(\theta)$ for 12 February 2010 at the ARM SGP site, when aerosols were the dominant particulate.

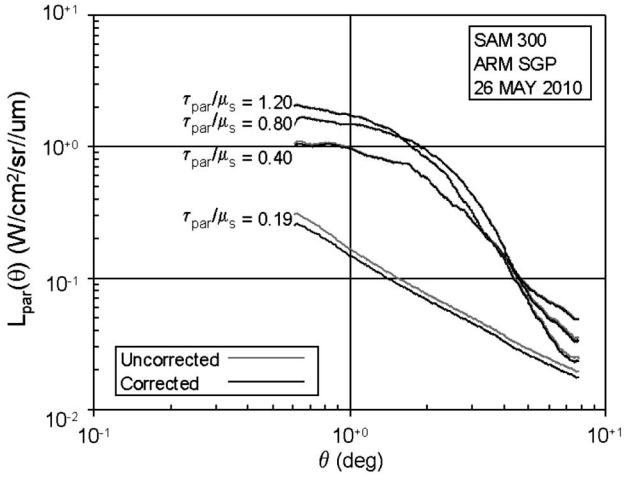

Fig. 14. Examples of uncorrected (gray) and corrected (black) particulate scattering profiles $L_{\text{par}}(\theta)$ for 26 May 2010, at the ARM SGP site. Three thin cumulus cases ($\tau_{\text{par}}/\mu_s = 1.20$, 0.80, and 0.21) are compared with an aerosol case ($\tau_{\text{par}}/\mu_s = 0.19$).

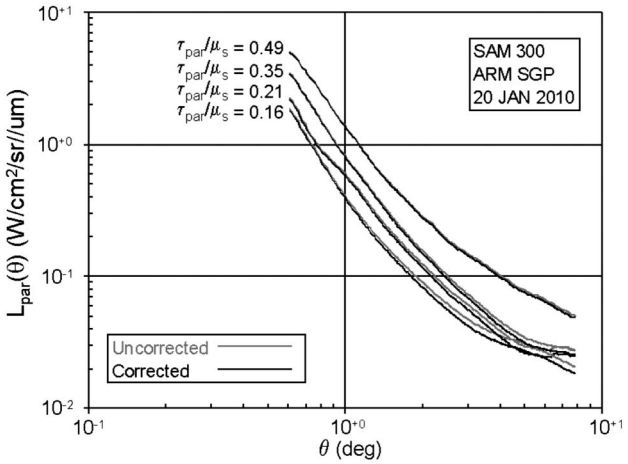

Fig. 15. Examples of uncorrected (gray) and corrected (black) particulate scattering profiles $L_{par}(\theta)$ for 20 January 2010 at the ARM SGP site. Four thin cirrus cases are shown.

of $n(a)$ attributable to not including internal scattering ranged from 10% larger for $\tau_{los} = 0.16$ to 2.5% larger for $\tau_{los} = 0.49$, with standard deviations of 10% and 3.8%, respectively.

6. Conclusion

We have presented two methods for determining instrumental internal scattering for correcting aureolegraph measurements of particulate scattering. The first, the BAS method, subtracts measurements made with and without an occluding ball that shades the aureolegraph from direct solar radiation. The second, which we have called the MLP method, involves extrapolating aureolegraph measurements collected through a large range of solar zenith angles. Although both methods require stable atmospheric particulate conditions over the course of the measurements, the BAS method takes only a fraction of an hour while the MLP method takes a large fraction of the daylight hours. In practice the requirement for stable conditions also means relatively clear conditions, i.e., low particulate optical depths. Nevertheless, the MLP method required the inclusion of provisions for changing particulate scattering phase functions over the course of the measurements. In principle the MLP method could be incorporated into the SAM automated data processing routine if criteria for judging when the aerosol conditions are sufficiently stable for the method to work properly could be developed. For example, we speculate that a good comparison between $S_{int}(\theta)$ based on pre- and post-noon data samples might provide such a criterion.

We compared internal scattering correction profiles obtained by the two methods using measurements from SAM #300 at the ARM SGP site on 8 January 2010. For scattering angles $\lesssim 4°$ the difference between the two is less than 20%. Internal scattering correction profiles obtained by the MLP method over the course of 5 months have power-law forms with similar slopes somewhat less negative than −2 but vary in magnitude by roughly a factor of 8. Since the required stability or regularity of the aerosol conditions poses a problem, we recommend use of the BAS method. Indeed, reasonably frequent collection of BAS datasets, when atmospheric conditions permit, would seem to be warranted until the stability of the internal scattering correction has been determined. If an intense, collimated laboratory source were available to simulate the solar irradiance, then it would be interesting to obtain a direct measurement of aureolegraph internal scattering without the complication of a long path through the atmosphere. A direct measurement from a high-altitude site in a clean environment, such as at Mauna Loa, Hawaii, would also be interesting.

We presented examples of aureole profile corrections for a variety of particulate layer types at the ARM SGP site using the BAS internal scattering profile for 8 January 2010. The aerosol example, 12 February, 2010, shows corrections for path optical depths ranging over a factor of 3.5. The corrections decrease with increasing optical depth and are largest at small angles (250%–170%) and smallest at large angles (21%–10%). The examples from 26 May 2010, compare three cases for fair weather cumulus clouds and one for aerosol. The corrections for the cumulus cases decrease with increasing optical depth and are largest at small angles (15% to 2%) and smallest at large angles (4%–1%). The examples from 20 January 2010 compare four cases for cirrus. The corrections for the cirrus cases also decrease with increasing optical depth, but are largest at large angles (13%–4%) and smallest at small angles (2%–1%).

For SAM's original application of retrieving the optical properties of thin clouds the corrections for aureolegraph internal scattering appear to be moderate (~15% or less) for cirrus and cumulus. For application in solar energy research [19], where aerosols are more important, the internal scattering corrections are also more important and the authors recommend fairly frequent determinations of the internal scattering profile, preferably using the BAS method. Such data would also be useful for investigating the time dependence of the internal scattering and correlating with maintenance operations (i.e., optics cleaning and protective plate replacement).

The authors note the support of their colleague Peter Baum in the development of the ball-and-stick method. They also acknowledge and thank the ARM program of the Department of Energy for hosting SAM #300 as a guest instrument at the SGP ARM Climate Research Facility. In particular, the authors thank Dan Rusk, operations manager, Tim Grove, Internet support, and Pat Dowell and Mark Klassen, technical assistants, at the SGP ACRF. The authors also thank Rick Wegener and his staff for their efforts in establishing and maintaining the AERONET instrument at the SGP ACRF. And last, but not least, the authors note their appreciation for the comments and questions of the anonymous reviewer.

References

1. F. Vilas and B. A. Smith, "Coronagraph for astronomical imaging and spectrophotometry," Appl. Opt. **26**, 664–668 (1987).
2. J. G. DeVore, A. T. Stair, A. LePage, D. Rall, J. Atkinson, D. Villanucci, S. A. Rappaport, P. C. Joss, and R. A. McClatchey, "Retrieving properties of thin clouds from solar aureole measurements," J. Atmos. Ocean. Technol. **26**, 2531–2548 (2009).
3. M. B. Lyot, "A study of the solar corona and prominences without eclipses," Mon. Not. R. Astron. Soc. **99**, 580 (1939).
4. N. T. O'Neill and J. R. Miller, "Combined solar aureole and solar beam extinction measurements. 1: calibration considerations," Appl. Opt. **23**, 3691–3696 (1984).
5. B. N. Holben, T. F. Eck, I. Slutsker, D. Tanré, J. P. Buis, A. Setzer, E. Vermote, J. A. Reagan, Y. J. Kaufman, T. Nakamima, F. Lavenu, I. Jankowiak, and A. Smirnov, "AERONET—a federated instrument network and data archive for aerosol characterization," Remote Sens. Environ. **66**, 1–16 (1998).
6. A. Ångström, "Apparent solar constant variations and their relation to the variability of atmospheric transmission," Tellus **22**, 205–218 (1970).
7. K. N. Liou, *An Introduction to Atmospheric Radiation*, 2nd ed. (Academic, 2002).
8. M. Nicolet, "On the molecular scattering in the terrestrial atmosphere: an empirical formula for its calculation in the homosphere," Planet. Space Sci. **32**, 1467–1468 (1984).
9. J. V. Dave, "Importance of higher order scattering in a molecular atmosphere," J. Opt. Soc. Am. **54**, 307–315 (1964).
10. A. Marshak and A. B. Davis, "Numerical methods," in *3D Radiative Transfer in Cloudy Atmospheres*, A. Marshak and A. B. Davis, eds. (Springer, 2005), pp 243–281.
11. I. M. Sobol, *A Primer for the Monte Carlo Method* (CRC Press, 1994).
12. D. Hestroffer and C. Magnan, "Wavelength dependency of the solar limb darkening," Astron. Astrophys. **333**, 338–342 (1984).
13. M. Born and E. Wolf, *Principles of Optics, Electromagnetic Theory of Propagation, Interference and Diffraction of Light* (Pergamon, 1959).
14. T. Nakajima, G. Tonna, R. Rao, P. Boi, Y. Kaufman, and B. Holben, "Use of sky brightness measurements from ground for remote sensing of particulate polydispersions," Appl. Opt. **35**, 2672–2686 (1996).
15. O. Dubovik and M. D. King, "A flexible inversion algorithm for retrieval of aerosol optical properties from Sun and sky radiance measurements," J. Geophys. Res. **105**, 20,673–20,696 (2000).
16. W. H. Press, S. A. Teukolsky, W. T. Vetterling, and B. P. Flannery, *Numerical Recipes in Fortran, The Art of Scientific Computing*, 2nd ed. (Cambridge, 1992).
17. J. G. DeVore, "Improved normalization of the size distribution of atmospheric particles retrieved from aureole measurements using the diffraction approximation," J. Atmos. Ocean. Technol. **28**, 1019–1027 (2011).
18. P. Yang, B. A. Baum, A. J. Heymsfield, H. Hu, H.-L. Huang, S.-C. Tsay, and S. Ackerman, "Single-scattering properties of droxtals," J. Quant. Spectrosc. Radiat. Transfer **79**, 1159–1169 (2003).
19. S. Wilbert, B. Reinhardt, J. DeVore, M. Röger, R. Pitz-Paal, and C. Gueymard, "Measurement of solar radiance profiles with the Sun and Aureole Measurement System (SAM)," in *Proceedings of the International SolarPACES Conference* (SolarPACES, 2011).